

EXPERIMENTAL VALIDATION OF HIGH POST-YIELD STIFFNESS DAMPERS FOR RESIDUAL DRIFT REDUCTION

Marco BAIGUERA^a, George VASDRAVELLIS^a, David REICHARDT^a and Theodore L.
KARAVASILIS^b

^a Institute for Infrastructure and Environment, Heriot-Watt University, Edinburgh, UK
Emails: mb311@hw.ac.uk, G.Vasdravellis@hw.ac.uk, dr29@hw.ac.uk

^b School of Engineering, University of Warwick, Coventry, UK
Email: T.Karavasilis@warwick.ac.uk

Keywords: Seismic Design; Residual drift mitigation; Seismic damper; Stainless steel; Cycling testing; Ductile fracture.

Abstract. *Seismic dampers made of duplex stainless steel with high post-yield stiffness have been recently proposed as the main energy-dissipative system in a dual steel frame. Nonlinear dynamic analyses have shown that these devices provide high post-yield stiffness to the frame, minimizing residual drifts and damage after a major earthquake. This paper presents the experimental evaluation of the proposed dampers. Monotonic and cyclic coupon tests were first conducted to characterise the hardening and fracture parameters of the material. Full-scale component tests were carried out on two prototype dampers using several cyclic loading protocols up to fracture. The results demonstrated that the dampers can withstand severe seismic input without failing, due to their excellent ductility and fracture capacity. Complementary numerical analyses were used to simulate the behaviour of the dampers and preliminary results are presented.*

1 INTRODUCTION

Recent earthquakes, such as the 2010/2011 Christchurch earthquakes, have shown that conventional steel frames designed according to current seismic provisions prevent collapse and ensure life safety. However, damage due to permanent deformations in main structural members was observed, resulting in some cases in high repair costs and excessive disruption to building use or occupation [1]. In order to improve the resilience of seismic-resistant steel structures, an effective design approach is to concentrate damage in steel yielding devices, protecting the main structural members and increasing the energy dissipation capacity of the structure. Different types of steel yielding devices have been proposed since the 1970s, such as U-shaped steel strips in flexure [2]. Dampers made of multiple steel plates with optimized shape, such as the added damping and stiffness (ADAS) flexural-beam damper [3], were developed and implemented in either eccentrically or concentrically braced frames. A triangular version of ADAS, known as T-ADAS, was proposed by Tsai and Li [4]. Other examples include the Kajima honeycomb damper implemented in Japan [5], the U-shaped steel strips, known as INERD connections, developed by Vayas and Thanopoulos [6] for concentrically braced frames, and the cast-iron yielding brace system proposed by Gray et al. [7].

Another major drawback of conventional steel systems is that they experience significant residual storey drifts following a strong seismic event. Residual storey drifts pose further complications: a recent study on the economic impact of residual drifts showed that direct and indirect repair costs are not financially viable when residual drifts are $>0.5\%$ [8,9]. Braced frames represent a system with enhanced seismic performance due to their high initial stiffness, which can effectively reduce storey drifts. However, conventional braced frames, such as concentrically braced frames (CBFs), exhibit a degrading hysteretic behaviour, which results in damage concentration to certain stories, fracture, and increased collapse potential. Buckling-restrained braced frames (BRBFs) represent an improved class of braced frames [10]. The buckling-restrained braces (BRBs) exhibit a stable hysteretic response and the ability to withstand significant ductility demands. They may be susceptible to large residual drifts and damage concentrations due to their low post-yield stiffness [11]. Previous analytical studies have shown that BRBFs designed according to current seismic codes do not meet the immediate occupancy performance level under the design-basis earthquake (10% probability of occurrence in 50 years; denoted as DBE), due to residual drifts greater than 0.5% [12]. Simple approaches to mitigate residual drifts have been studied in [13]. Among these, providing high post-yield stiffness is recognized as an effective strategy to reduce residual drifts.

A dual seismic-resistant steel frame, which consists of a moment-resisting frame equipped with concentric braces, has been recently proposed and numerically evaluated by the authors [14]. High post-yield stiffness is provided by yielding devices made of duplex stainless steel, which are installed in series with the braces. This paper presents the experimental validation of the proposed dampers. The results of sixteen full-scale component tests conducted using two geometries and different cyclic loading protocols are presented. The load histories are representative of earthquake loadings. The hysteretic behaviour and fracture capacity are assessed. The hardening and fracture parameters of duplex stainless steel are also evaluated using monotonic and cyclic tests on round and circumferentially notched bars. Complementary finite element models of the seismic dampers and coupon specimens are developed and validated against the experimental tests.

2 PROTOTYPE DUAL CBF-MRF

Figure 1a shows the configuration of the dual system proposed by Baiguera *et al.* [14]. A moment resisting frame (MRF) equipped with concentric braces, denoted as dual CBF-MRF, uses simple structural details to provide enhanced seismic performance, *i.e.*: a) seismic dampers made of duplex stainless steel (SSD) with high post-yield stiffness, designated as SSD-WHPs, are placed in series with the concentric braces; and b) replaceable fuses are placed at the locations of the beams where plastic hinges are expected to develop. WHPs were previously used in a steel beam-column post-tensioned connection for self-centering MRFs as the main energy dissipation system [15]. Component tests conducted in that study as well as cyclic and monotonic tests performed in [16] showed that WHPs made of duplex stainless steel possess the most favourable performance for seismic design. SSD-WHPs also have a high post-yield stiffness, which contributes to reduce residual drifts after a strong earthquake [13]. Therefore, SSD-WHPs are used in the proposed CBF-MRF and additional tests are carried out to further evaluate their seismic response in a braced frame.

The SSD-WHPs are installed only at one end of the braces and pass through aligned holes between the gusset plate and a strong U-shaped plate, which is connected by either welding or bolting to the brace member (figure 1b). SSD-WHPs are hourglass shape steel yielding devices that dissipate energy due to bending inelastic deformations. The geometric properties of the bending part of a SSD-WHP are shown in figure 2. The internal parts have length L_{WHP} , external

diameter D_e , and mid-length diameter D_i . The internal part is assumed to have fixed boundary conditions as it bends. The hourglass shape promotes a constant curvature profile and a uniform distribution of plastic deformations to delay fracture and increase energy dissipation [16].

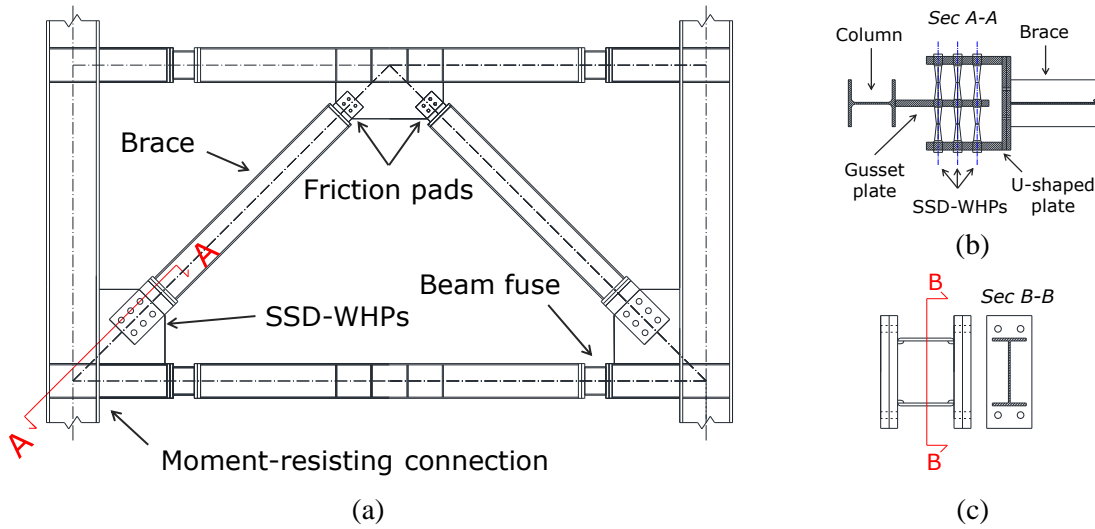


Figure 1: Geometry of the proposed dual CBF-MRF: a) overview; b) brace-damper connection detail; and c) beam fuse detail

Replaceable fuses are placed in the main beams immediately after the gusset plates, where plastic hinges are expected to develop, as shown in figure 1a. They are designed following the same concept of the replaceable link proposed by Shen et al. [17]. The fuses are smaller than the main beam steel I-sections, welded on strong end plates, which in turn are bolted on the main beam (figure 1c).

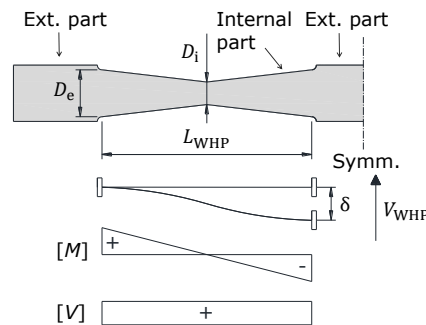


Figure 2: SSD-WHP: geometry, deflection, elastic bending moment, and shear diagram

The proposed CBF-MRF has high post-yield stiffness as a result of the SSD material behaviour. In order to ensure that the structure meets the capacity design requirements, friction pads are placed between the brace members and the beam gusset plates at the top of each floor, as illustrated in figure 1a. They are activated at a predefined storey drift level (e.g., 3% roof drift).

A 6-storey prototype building with three equal bays in each direction was designed according to the provisions of Eurocodes 3 [18] and 8 [19] using as seismic-resistant system the proposed CBF-MRF. The bay width and the storey height are 6 m and 3 m, respectively. A performance-based seismic design procedure was used to design the dual frame, and details are contained in [14]. The seismic performance of the dual frame was evaluated with advanced numerical simulations using experimentally validated shell-solid finite element models and simplified beam element models. The numerical results showed that the dual frame had adequate stiffness

and energy dissipation capacity to control peak storey drifts (i.e. non-structural damage), while plastic deformations (i.e. structural damage) were isolated within the SSD-WHPs and the beam fuses. In addition, the high post-yield stiffness of the SSD-WHPs, combined with the appreciable elastic deformation capacity of the moment-resisting frame, resulted in significant reduction of residual storey drifts, which were found to have a mean value of 0.06% under the DBE and a mean value of 0.12% under the maximum considered earthquake (2% probability of exceedance in 50 years; denoted as MCE), as described in detail in [14]. These values indicate a superior residual storey drift performance compared to steel frames equipped with buckling restrained braces, and highlight the potential of the proposed dual frame to help steel buildings to return to service within an acceptable short time in the aftermath of a strong earthquake.

3 EXPERIMENTAL PROGRAMME

An extensive testing programme was conducted to evaluate the seismic behaviour of the SSD-WHPs using similar loading and support conditions as expected in a braced frame.

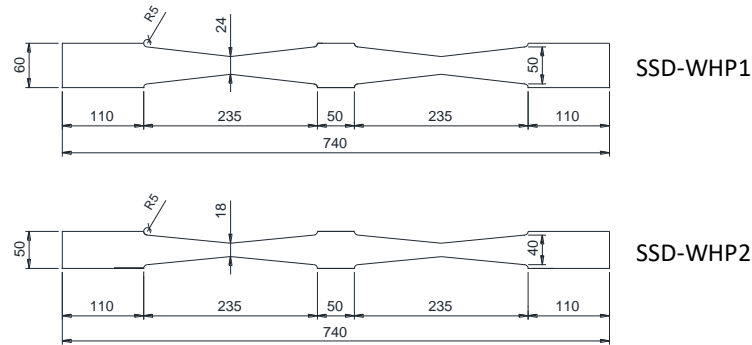


Figure 3: Geometry of the test specimens (all dimensions in mm)

3.1 Test specimens

Full-scale tests on SSD-WHPs were carried out in order to investigate their seismic performance and fracture capacity. Figure 3 shows the geometry of the specimens, which are representative of the SSD-WHP geometries at the first and last three stories of the 6-storey prototype building. The first geometry (large SSD-WHP) has $D_e = 50$ mm, $D_i = 24$ mm, and $L_{WHP} = 225$ mm, while the second one (small SSD-WHP) has $D_e = 40$ mm, $D_i = 18$ mm, and $L_{WHP} = 225$ mm. The two geometries are denoted as SSD-WHP1 and SSD-WHP2, respectively. The specimens have been fabricated to have a minimum clearance (i.e., 0.2 mm) between their external surfaces and the holes of the supporting plates (figure 4). In order to axially restrain the SSD-WHPs, steel washers were welded to the external parts of the pin (figure 5b).

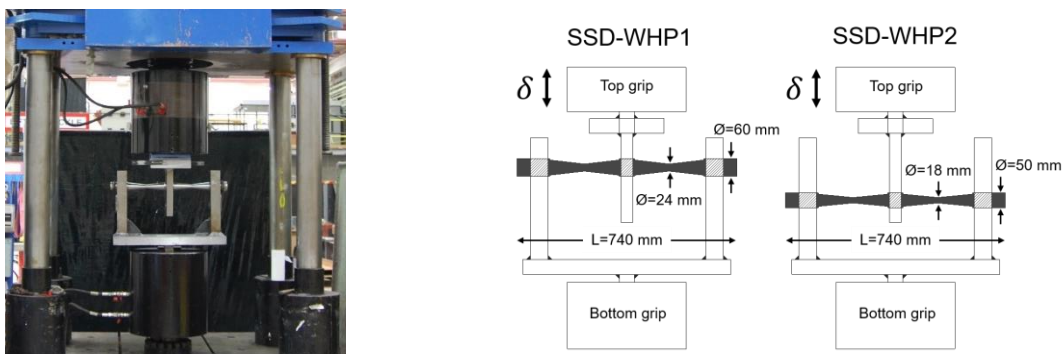


Figure 4: Test setup

3.2 Testing apparatus and instrumentation

The component tests were performed using a Losenhausen UPS200 (LOS) testing machine. It has 2000 kN force capacity in tension and compression, with 250 mm displacement capacity. The SSD-WHPs were tested in a configuration reproducing the actual layout of the brace-damper connection (see figure 1b). The specimen was inserted into aligned holes drilled on external supporting plates (named as lower plates) and on an internal plate (named as upper plate), as shown in figure 4. These plates correspond to the gusset plates in the proposed brace-damper connection.

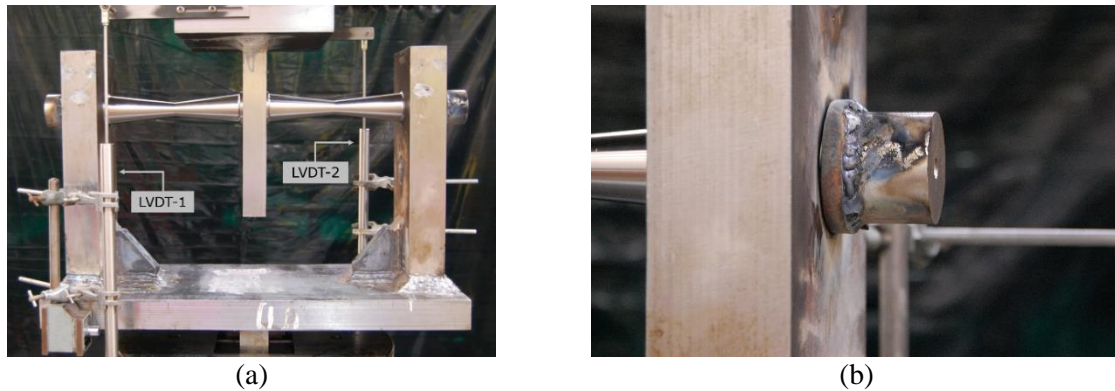


Figure 5: (a) Test instrumentation; and (b) welded collars for axial constraint

Two linear variable differential transformers (LVDTs) were attached to the lower plate by magnetic bases, with their tip pinned to a nail attached to the upper plate, as shown in figure 5a. They were used to measure the relative displacement between the lower and upper plates.

3.3 Material properties and fracture parameters

Coupon tests were conducted to characterize the properties of the SSD material. Tensile tests were carried out on round bars to evaluate the mechanical properties of SSD (e.g., yield stress, post-yield properties, and ductility). In addition, circumferentially-notched specimens (CNSs) were tested under monotonic and cyclic loading protocols in order to investigate the ductile fracture under axisymmetric stress states with high triaxiality. The geometry of the coupon specimens is shown in figure 6.

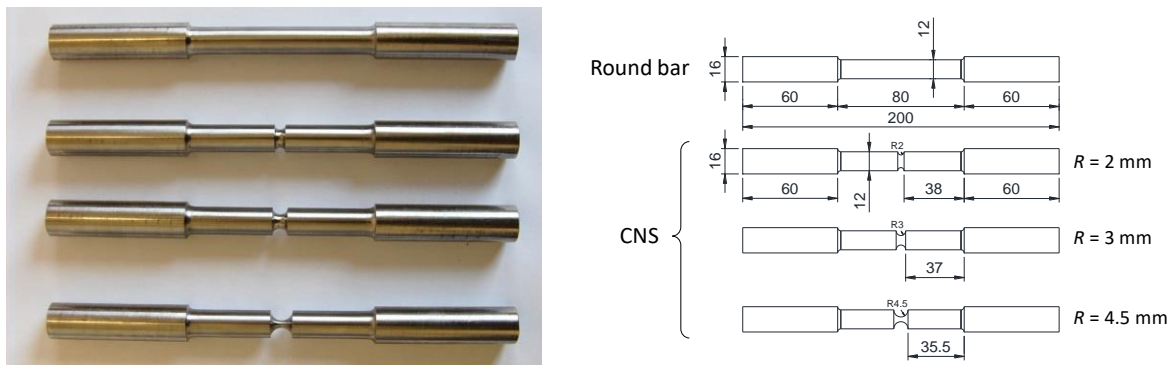


Figure 6: Geometry of the coupon specimens (all dimensions in mm)

The coupon specimens were tested using an Instron 8803 testing machine with a maximum load capacity of 600 kN. The coupons were loaded axially and were gripped using vee-serrated jaw faces. A contact extensometer having a gauge length of 50 mm was used for the strain measurements and was located in the centre of the specimen (figure 7a). The specimens were loaded at a rate of 1 mm/min through a displacement-controlled testing protocol. In order to

protect the extensometer from being damaged by the sudden fracture of the specimen, it was removed after necking, as shown in figure 7b.



Figure 7: Coupon test setup: (a) extensometer with 50 mm gauge length; and (b) necking

Table 1: Summary of mechanical properties of SSD

Coupon	f_y [MPa]	f_u [MPa]	ϵ_f [%]	E [MPa]
Round bar 1	530	752.4	45.7	189,655
Round bar 2	513	750.9	47.5	181,250
Round bar 3	518	745.8	47.9	187,500
Average	520	749.7	47.0	186,135

3.3.1 Round bars

Three uniaxial tensile tests were carried out on round bars, which were designed in accordance with EN 1002-1 [20]. As shown in figure 6, the tested specimens have a nominal external diameter of 16 mm and are tapered to a reduced diameter of 12 mm. Fracture was observed in all the three tests. Table 1 summarizes the mechanical properties of SSD obtained from each test, i.e., the yield stress f_y (defined by the 0.2% offset strain), the ultimate stress f_u , the elongation at fracture ϵ_f , and the Young's modulus E . Figure 8a shows the force-displacement curves from the tensile tests and figure 9a shows the corresponding stress-strain curves.

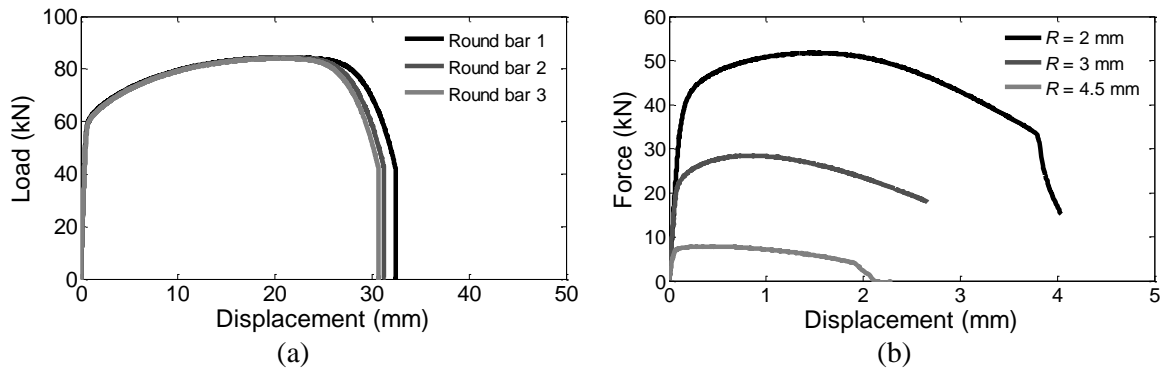


Figure 8: Load-displacement curves from tensile tests: (a) round bars; and (b) CNSs

The results show that SSD has an average yield stress equal to 520 MPa, which is 15% higher than the minimum nominal value of S31803/S32205 duplex stainless steel (450 MPa). Figure 9a shows that SSD is characterised by large ductility and high post-yield stiffness. The ratio of the post-yield stiffness to the elastic stiffness is 1/125. The engineering stress-strain curve is used to define the true stress-strain curve (figure 9b), which provides a true representation of the material behaviour and the input for the material properties as required by finite element (FEM) software.

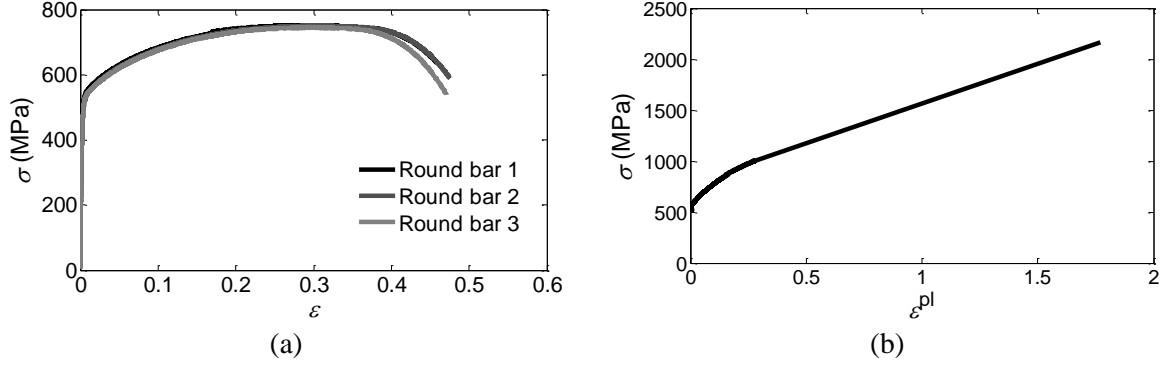


Figure 9: (a) Engineering stress-strain curves from tensile tests; and (b) true stress-strain curve

3.3.2 Circumferentially-notched specimens

CNSs were tested to investigate the ductile fracture parameters under axisymmetric stress states with high triaxiality [21]. Three different radii were used, i.e. $R = 2, 3,$ and 4.5 mm (figure 6b) to create the notch, thus introducing three different levels of triaxiality. For each geometry, three specimens were tested under monotonic tensile loading. Cyclic protocols were also used since they are more representative of earthquake loadings. As summarized in table 2, increasing amplitude and constant amplitude (CA) tests were performed under displacement control, based on the measurement from the extensometer with a loading rate of 1 mm/min.

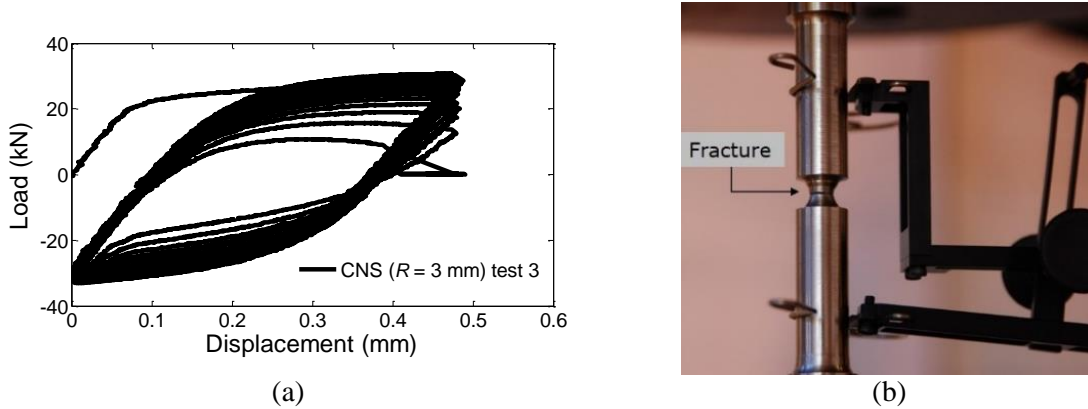

 Figure 10: CA test on CNS ($R = 3$ mm): (a) load-displacement curve; and (b) ductile fracture

Table 2: Cyclic loading protocols for CNSs

CNS	Test	Loading protocol
$R = 2$ mm ($u_y = 0.14$ mm)	1	$(4)x[0;4u_y]+(4)x[0;6u_y]+(4)x[0;8 u_y]$
	2	$(22)x[0;5u_y]$
	3	$(24)x[0;6u_y]$
$R = 3$ mm ($u_y = 0.094$ mm)	1	$(4)x[0;4u_y]+(4)x[0;6u_y]+(4)x[0;8u_y]+(4)x[0;10u_y]+(1) x[0;12u_y]$
	2	$(21)x[0;8u_y]$
	3	$(39)x[0;5u_y]$
$R = 4.5$ mm ($u_y = 0.063$ mm)	1	$(41)x[0;5u_y]$
	2	$(4)x[0;4u_y]+(4)x[0;6u_y]+(4)x[0;8u_y]+(4)x[0;10u_y]+(2)x[0;12u_y]$
	3	$(19)x[0;8u_y]$

Note: the number in parentheses indicates the number of cycles, followed by the prescribed cyclic amplitude in square brackets. For example, $(22)x[0;5u_y]$ refers to a specimen subjected to twenty-two cycles between 0 and 5 times u_y .

3.4 Loading protocols

Specimens SSD-WHP1 and SSD-WHP2 were tested under different loading protocols, which are listed in table 4. The AISC protocol is derived from ANSI/AISC 341-10 Annex K [22], and it is intended for the validation of buckling-restrained braces. It can be used for the proposed dampers, since they are designed to provide a full and stable hysteresis to the bracing members, yielding in both tension and compression. This loading protocol, presented in table 3, is defined by the yield displacement Δ_{by} and the DBE brace demand Δ_{bm} , which are determined in the pushover simulations described in detail in [14]. The displacement demands are $\Delta_{bm} = 17$ mm for SSD-WHP1 (i.e., the demand at the third storey of the prototype frame), and $\Delta_{bm} = 14$ mm for SSD-WHP2 (i.e., the demand at the top storey).

Table 3: AISC protocol

Phase	No of cycles	Amplitude (mm)	
		SSDWHP1	SSDWHP2
1	2	Δ_{by}	8
2	2	$0.5\Delta_{bm}$	8.5
3	2	Δ_{bm}	17
4	2	$1.5\Delta_{bm}$	25.5
5	2	$2\Delta_{bm}$	34

In order to assess the behaviour of SSD-WHPs under ultra-low cycle fatigue, CA protocols were used. The imposed displacements were equal to $4u_y$ (i.e., 4 times the yield displacement), $5u_y$, $6u_y$, and $7u_y$. Specimen SSD-WHP2 was subjected to one more CA test at $8u_y$. In addition, cyclic protocols with randomly-generated number of cycles and amplitude were used. Figure 11 shows the random protocols applied to SSD-WHP1 specimens. Monotonic loading was also used to evaluate the ultimate behaviour of SSD-WHPs. The displacement-controlled protocols were applied at a rate ranging from 5 to 40 mm/min, depending on the imposed amplitude.

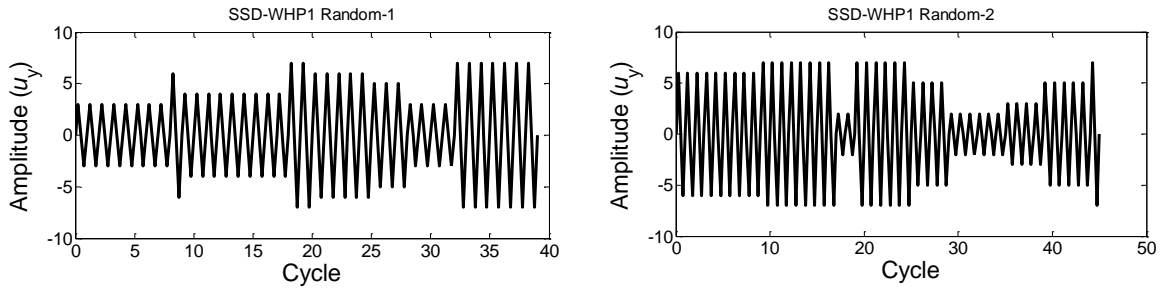


Figure 11: Random loading protocols

4 EXPERIMENTAL RESULTS

Sixteen full-scale component tests were conducted, as summarized in Table 4. For both the specimens, the AISC tests were first performed, followed by a set of CA tests and random tests. Finally, monotonic tests were conducted to assess the ultimate performance of the dampers under very large displacements.

Figure 12 shows the force-displacement curves of SSD-WHP1 and SSD-WHP2 under the AISC protocol. Both the specimens successfully met the intended displacement history, showing stable and full hysteresis. No cracks or early deterioration were observed. The hysteresis of the SSD-WHPs is characterized by a slight pinching at zero force, due to the small clearance that allows the pins to slip.

Table 4: Test matrix for full-scale component tests

Specimen	u_y (mm)	F_y (kN)	Test	Test protocol	No of cycles	Failure mode
SSD-WHP1	7	160	1	AISC	10	No failure
			2	CA at $7u_y$	28	Ductile fracture
			3	CA at $6u_y$	35	Ductile fracture
			4	CA at $5u_y$	43	Ductile fracture
			5	CA at $4u_y$	78	Ductile fracture
			6	Random-1	59	Ductile fracture
			7	Random-2	45	Ductile fracture
			8	Monotonic	-	No failure
SSD-WHP2	7	75	9	AISC	10	No failure
			10	CA at $8u_y$	33	Ductile fracture
			11	CA at $7u_y$	42	Ductile fracture
			12	CA at $6u_y$	59	Ductile fracture
			13	CA at $5u_y$	76	Ductile fracture
			14	CA at $4u_y$	89	Ductile fracture
			15	Random	49	Ductile fracture
			16	Monotonic	-	No failure

The deformed shape of SSD-WHPs, illustrated in figure 13, shows their large ductility under bending. The hourglass shape that promotes a uniform distribution of plastic deformations provided large energy dissipation and delayed fracture. Based on the results from the AISC tests, the yield displacement u_y was assumed 7 mm for both the specimens.

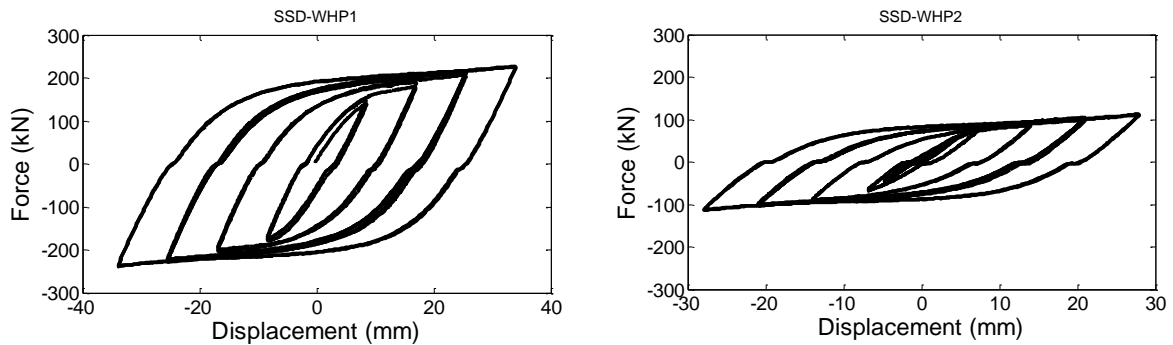
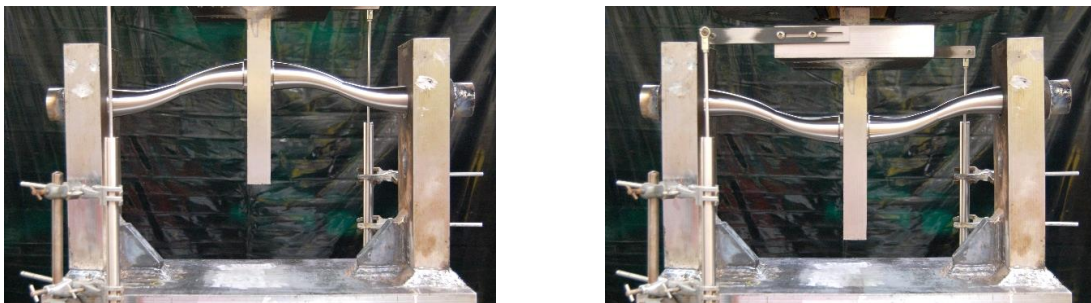


Figure 12: Hysteretic behaviour of SSD-WHP1 and SSD-WHP2 under AISC protocol

Figure 14 illustrates the force-displacement response of SSD-WHP1 and SSD-WHP2 under two constant amplitude protocols ($5u_y$ and $7u_y$), which are representative of the CA test set. The results indicate that SSD-WHPs have stable hysteretic behaviour and large fracture capacity. Under the CA protocols at 49 mm ($7u_y$) and 35 mm ($5u_y$), SSD-WHP1 reached full fracture after 28 and 43 cycles, while SSD-WHP2 fractured after 42 and 76 cycles. The cyclic envelopes from CA tests show significant hardening, especially under large imposed displacements.


 Figure 13: Deformed shape of SSD-WHP1 at ± 49 mm ($7u_y$) under Random-1 protocol

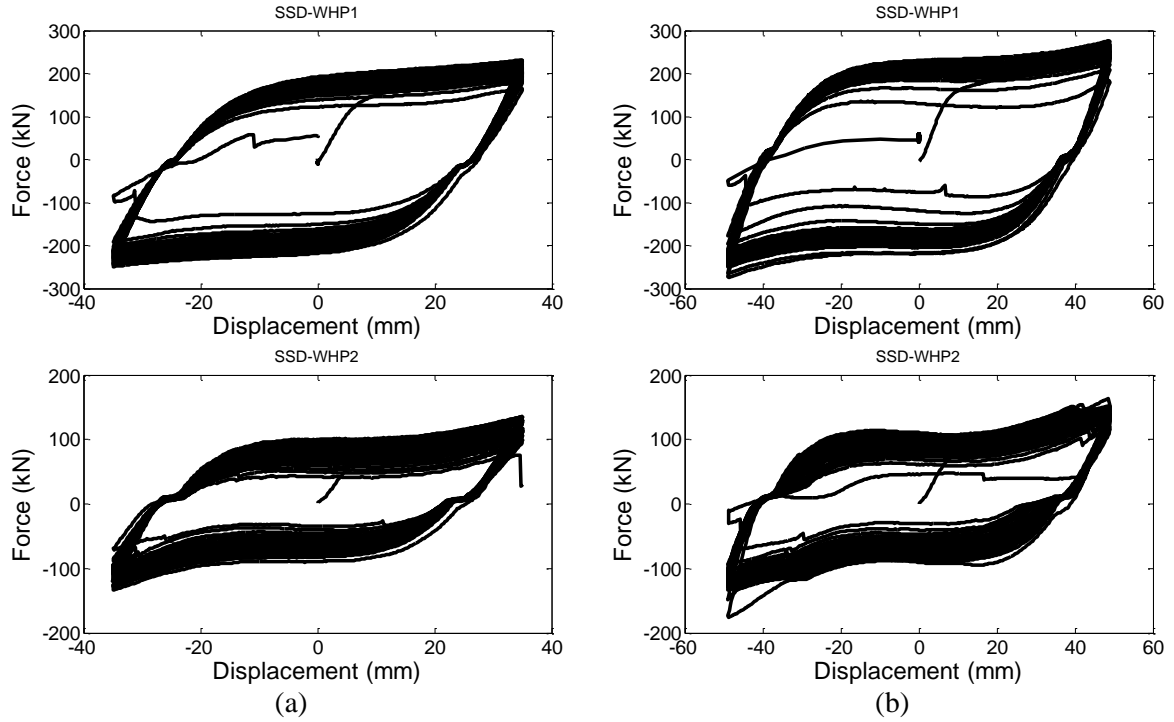


Figure 14: Hysteresis of SSD-WHP1 and SSD-WHP2: (a) CA tests at $5u_y$; and (b) CA tests at $7u_y$;

The CA tests were performed to study the ultra-low cycle fatigue of the seismic dampers. The results summarized in table 4 are used to calibrate the parameters of a Coffin-Manson equation that correlates the imposed displacement amplitude, Δ_f , to the number of cycles applied to reach fracture, N_f [16]:

$$\Delta_f = \Delta_0 \times (N_f)^m \quad (1)$$

The estimated values of Δ_0 and m are 350 mm and -0.6 for SSD-WHP1 (figure 16a), and 455 mm and -0.6 for SSD-WHP-2 (figure 16b).

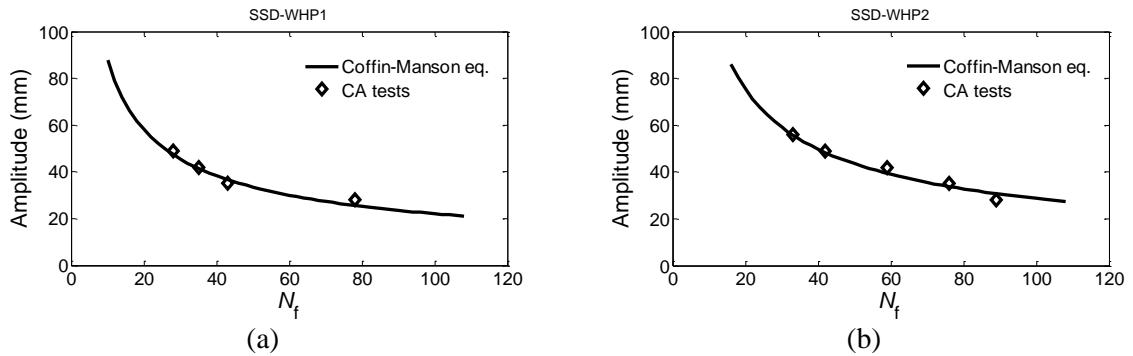


Figure 16: Low-cycle fatigue life of SSD-WHPs

The low-cycle fatigue curves are also used to approximately estimate the failure of SSD-WHPs under loading protocols of variable amplitude. The Palmgren-Miner linear damage accumulation rule is used:

$$D = \sum_{i=1}^j \frac{n_i}{N_{f,i}} \quad (2)$$

where n_i is the number of cycles applied at a given amplitude, $N_{f,i}$ is the number of cycles applied at a given amplitude to reach fracture, and D is the damage index, which is equal to 1 when the fatigue life is reached [11]. As shown in table 5, the experimental fracture of SSD-WHP1 and SSD-WHP2 under two different random protocols occurs at end of phases 14 and 9, where Miner's rule gives a value of D equal to 1.14 and 0.99, respectively. Therefore, the damage accumulation computed using a linear rule provides an acceptable agreement with the experimental results. The estimation of the Coffin-Manson equation parameters along with the use of Miner's rule is useful for the development of FEM models that incorporate the fracture of SSD-WHPs. For example, in OpenSees [23] the fatigue material model, which accounts for the effects of low cycle fatigue, uses the Miner's rule, based on Coffin-Manson relationships, and it can be incorporated in a spring-like model that simulates the behaviour of the seismic damper.

Table 5: Miner's linear damage rule

Phase	SSD-WHP1 Random-1				SSD-WHP2 Random			
	Δ_f	n	N_f	D	Δ_f	n	N_f	D
1	$3u_y$	8	109	0.07	$6u_y$	9	59	0.15
2	$6u_y$	1	35	0.10	$7u_y$	8	42	0.34
3	$4u_y$	9	78	0.22	$8u_y$	2	33	0.40
4	$7u_y$	2	28	0.29	$7u_y$	6	42	0.55
5	$6u_y$	5	35	0.43	$5u_y$	4	76	0.60
6	$5u_y$	3	43	0.50	$8u_y$	6	33	0.78
7	$3u_y$	4	109	0.54	$3u_y$	4	168	0.80
8	$7u_y$	7	28	0.79	$5u_y$	5	76	0.87
9	$3u_y$	2	109	0.81	$7u_y$	5	42*	0.99
10	$7u_y$	3	28	0.91				
11	$3u_y$	2	109	0.93				
12	$4u_y$	2	78	0.96				
13	$2u_y$	4	214	0.98				
14	$5u_y$	7	43*	1.14				

*Experimental fracture

Figure 17a illustrates the fracture mode of SSD-WHPs. Extensive plastic deformations due to bending concentrated in Sections 1 (close to the upper plate) and 2 (close to the lower plate). After several cycles, cracks propagated in those sections. Figures 17b and 18b show the final cycle of SSD-WHP1 under Random-2 test protocol and SSD-WHP2 under CA protocol at 28 mm. The specimens eventually failed due to complete fracture in Section 2.

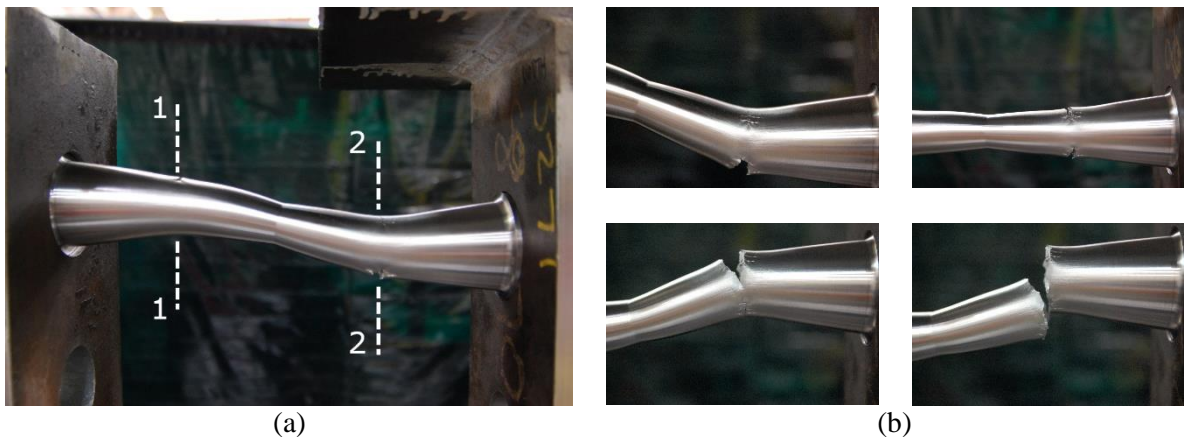


Figure 17: Fracture of SSD-WHP1 (Random-2 test): (a) fracture locations; and (b) final cycle



Figure 18: SSD-WHP2 (CA test at $4u_y$): (a) axial expansion; and (b) final cycle with full fracture

Due to extensive plastic deformations spread over the length of the steel pins, a significant axial expansion was observed, as illustrated in figure 18a. After several cycles, this expansion was large, in the range of 15-20 mm for SSD-WHP1 and 30-40 mm for SSD-WHP2. This is in agreement with the experimental observations: cracks were spread on a larger area in SSD-WHP2 (figure 19) than in SSD-WHP1 (figure 17b), where a single large crack propagated.

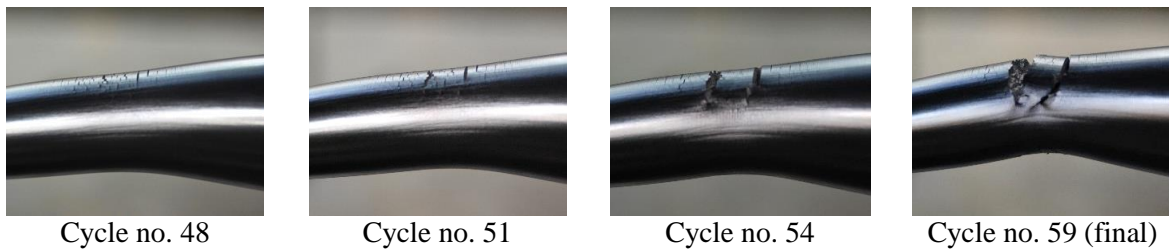


Figure 19: CA test at $6u_y$: fracture evolution

The monotonic behaviour of SSD-WHP1 is illustrated in figure 20a. It exhibited a high post-yield stiffness, equal to 1/10 of the elastic stiffness. Figure 20b shows the specimen at 110 mm imposed displacement, which corresponds to 6.5 times Δ_{bm} . At this displacement the test was stopped, since no fracture of the SSD-WHP1 occurred. The lower supporting steel plates sustained significant bending, without weld failure. A similar behaviour was observed for SSD-WHP2, which exhibited a post-yield modulus equal to 2/10 of the elastic modulus. The excellent ductility of the SSD-WHPs under excessive monotonic loading suggests that they represent a potentially superior way to provide increased robustness under progressive collapse of the frame, on top of their excellent seismic performance.

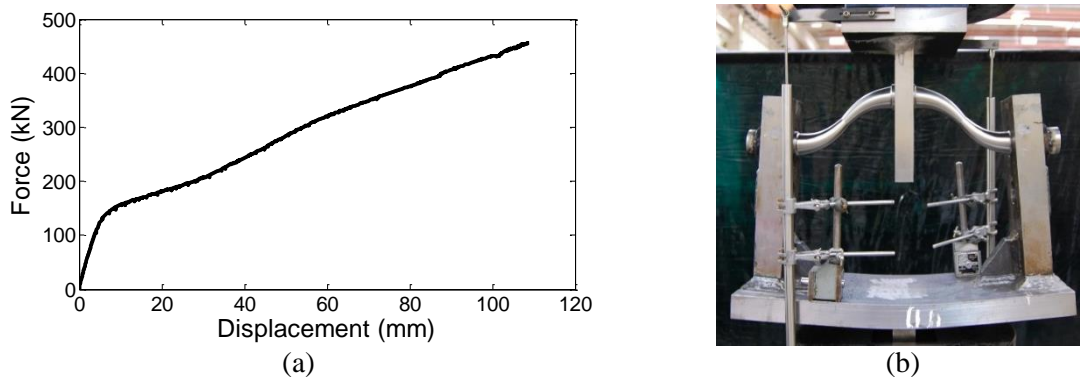


Figure 20: SSD-WHP1 monotonic test: (a) force-displacement behaviour; and (b) deformed shape at 110 mm displacement

5 NUMERICAL SIMULATIONS

5.1 Calibration of SSD cyclic hardening model

Numerical simulations were carried out to calibrate the material properties that define the cyclic plastic behaviour of SSD. Nonlinear FEM models of CNSs were created using the commercial software Abaqus [24]. Figure 21 shows the geometry of the model, which reproduces the gauge length section and takes into account the symmetry of the specimen. Elements with reduced integration, namely CAX4R in Abaqus, were used. A refined mesh was applied in the notch region with an element size of 0.25 mm, as recommended by Kanvinde and Deierlein [25]. The extensometer displacement history was applied to the FEM model.

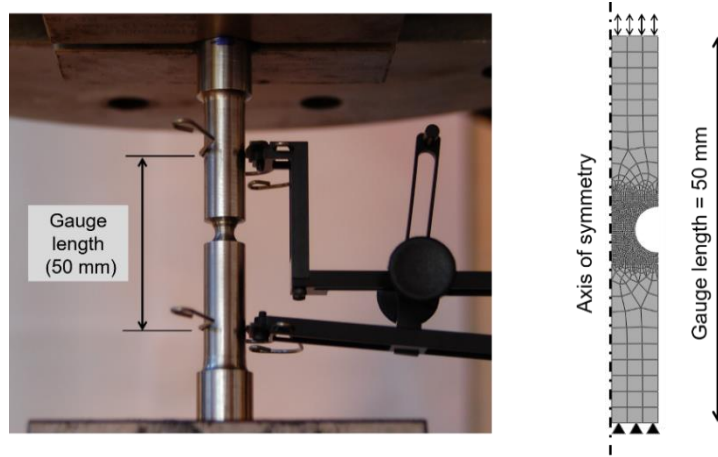


Figure 21: Axisymmetric FEM model of CNS with $R = 3$ mm

The accuracy of the FEM model was first assessed by simulating the CNS tensile tests. An isotropic hardening model was defined using the true stress-strain curve obtained from the tensile tests on round bars (figure 9b). The comparison of the numerical and experimental force-displacement curves for all the three CNSs is illustrated in figure 22. A good agreement is found for CNSs with $R = 2$ and 3 mm, where the results for CNS with $R = 4.5$ mm show significant differences between the experimental and numerical curves. Small geometry inconsistencies in the notch region and hardening due to the tapering process might have influenced the experimental results.

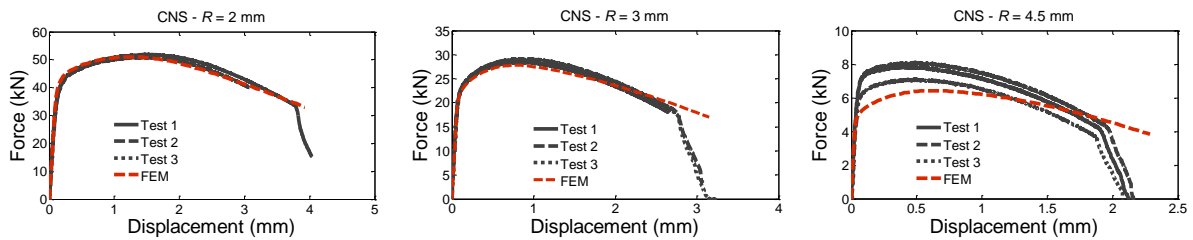


Figure 22: CNS tensile tests: experimental-numerical comparison

The hysteretic behaviour of SSD is simulated by an elastoplastic material model with combined isotropic and kinematic hardening. The material model is defined by the yield surface $\varphi(\boldsymbol{\sigma})$ defined as [24]:

$$\varphi(\boldsymbol{\sigma}) = \sqrt{\frac{3}{2}(\boldsymbol{S} - \boldsymbol{\alpha})^t(\boldsymbol{S} - \boldsymbol{\alpha})} - \sigma^0 \quad (3)$$

where σ^0 is the yield stress, t is the transposition operation, S is the stress deviator, σ is the stress vector and α is the backstress vector. The hardening laws for each backstress are defined as:

$$\alpha = \sum_{k=1}^B \alpha_k \quad (4)$$

$$\dot{\alpha}_k = \frac{C_k}{\sigma^0} (\sigma - \alpha) \dot{\bar{\epsilon}}^p - \gamma_k \alpha_k \dot{\bar{\epsilon}}^p \quad (5)$$

where a superimposed dot indicates an incremental quantity, B is the total number of the backstresses, C_k and γ_k are the constitutive material parameters to be calibrated against the experimental results, and $\dot{\bar{\epsilon}}^p$ is the equivalent plastic strain rate. The evolution of σ^0 (isotropic hardening component) is defined by the following exponential law:

$$\sigma^0 = \sigma|_0 + Q_\infty (1 - e^{-b\bar{\epsilon}^p}) \quad (8)$$

where $\sigma|_0$ is the yield stress at zero plastic strain, b defines the rate at which the size of $\varphi(\sigma)$ changes for increasing plastic strains, and Q_∞ is the maximum change in the size of $\varphi(\sigma)$.

Several simulations were conducted to identify the values of the parameters that define the aforementioned constitutive model. A good agreement is achieved adopting the following values: $\sigma|_0 = 400$ MPa, $C_1 = 6,500$ MPa, $\gamma_1 = 30$, $C_2 = 100,000$ MPa, $\gamma_2 = 700$, $b = 5$, $Q_\infty = 200$ MPa. Figure 23 shows the experimental and FEM simulated hysteretic behaviour from cyclic tests on CNS with $R = 2$ and 3 mm.

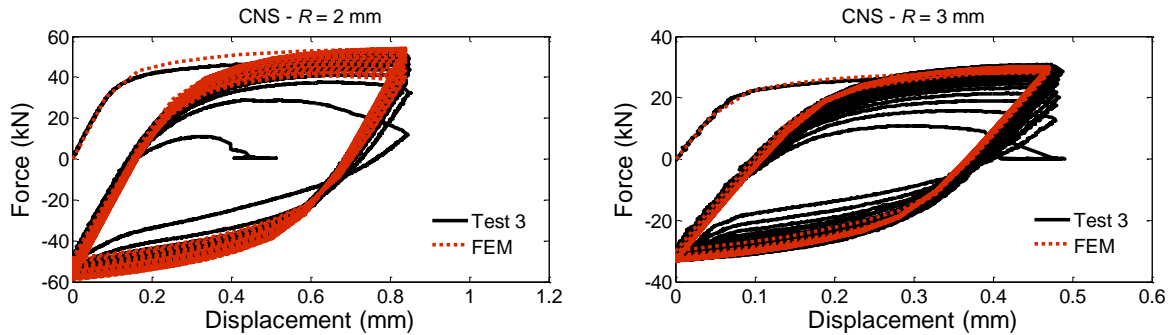


Figure 23: CNS cyclic tests: experimental-numerical comparison

5.2 SSD-WHP1 model

A three-dimensional FEM model was developed in Abaqus Explicit to simulate the hysteretic behaviour of SSD-WHP1. Figure 24 shows an overview of the FEM model along with the boundary conditions. Only half of the test setup was reproduced in full detail due to its symmetric geometry. The SSD-WHP1 and the supporting steel plates were modelled using solid elements with reduced integration, namely C3D8R. The mesh density is more refined in the SSD-WHP1 than in the steel plates, as shown in figure 24. The general contact algorithm was used to define the interaction between the external surfaces of SSD-WHP1 and the holes of the supporting plates. A contact property with normal and tangential behaviour was applied, assigning a friction coefficient of 0.2. In order to capture the pinching behaviour at zero force observed in the experimental force-displacement curves (figures 12 and 14), a small clearance, equal to 0.2 mm, was left between the SSD-WHP1 and the surrounding holes.

Displacement-controlled analyses were conducted under quasi-static loading conditions in the large displacement/strain nonlinear regime. For a first calibration of the model, the CA test at $7u_y$ (i.e., 28 cycles at 49 mm) was simulated. The cyclic loading protocol was applied to the upper supporting plate. To avoid dynamic effects, the loading rate used was relatively low (3 mm/s). In order to ensure a stable analysis, the density of the material was decreased and the displacement history was applied with a periodic amplitude. The material hardening parameters calibrated for SSD were adopted.

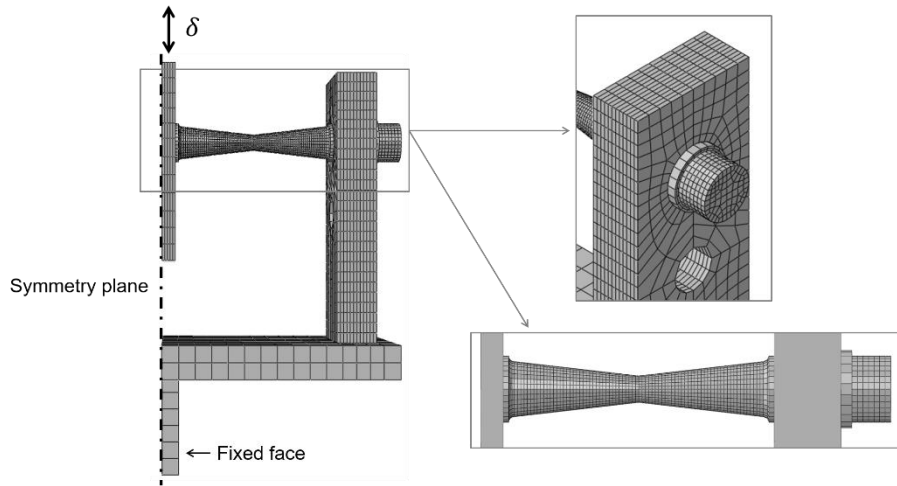


Figure 24: FEM model of half of a SSD-WHP1

Figure 25a shows the contour plots of the equivalent plastic strain on the deformed shapes of the SSD-WHP1 and the steel plates at 49 mm imposed displacement, along with a comparison with the experimental test. As illustrated in figure 25b, the maximum PEEQ is located at the centre of the half bending part (Sections 1 and 2), where fracture initiation and evolution was experimentally observed (figure 17). The FEM model was able to capture the axial expansion due to extensive plastic deformations (figure 25c), in agreement with the experimental observations (figure 18a).

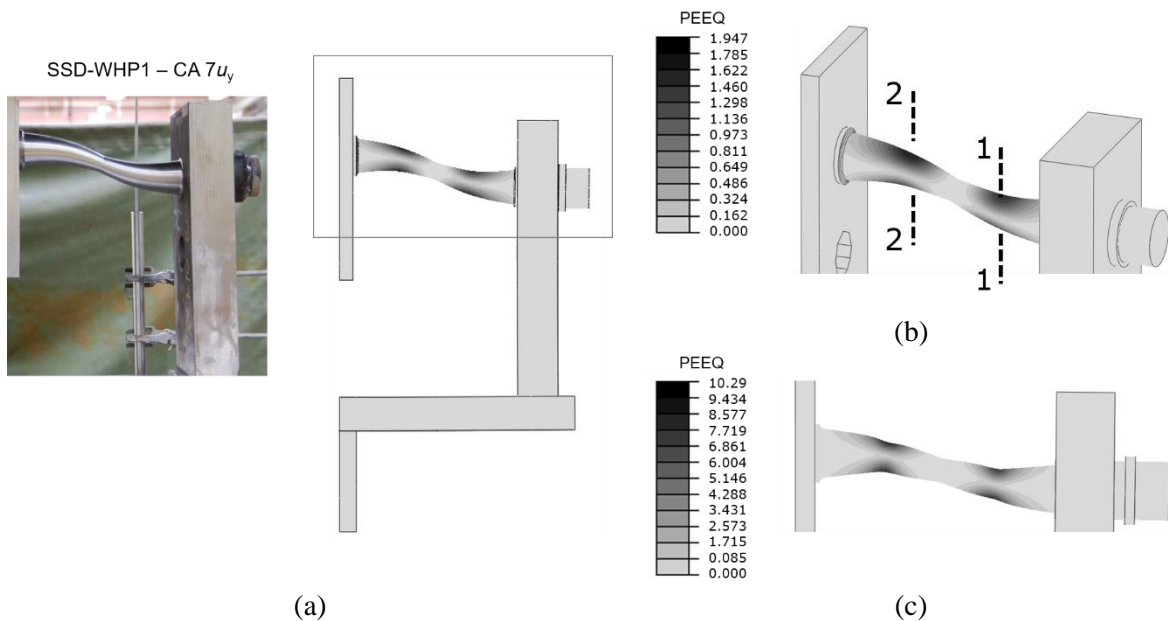


Figure 25: (a) Numerical and experimental deformed shape of SSD-WHP1; (b) PEEQ contour plots after 10 cycles; and (c) PEEQ contour plots after 19 cycles

Figure 26 plots the force-displacement hysteresis of the FEM model against the experimental curve. The results indicate that FEM model is capable of tracing the nonlinear cyclic behaviour of SSD-WHP1 with good accuracy. The pinching effect at zero force due to the small clearance was captured accurately.

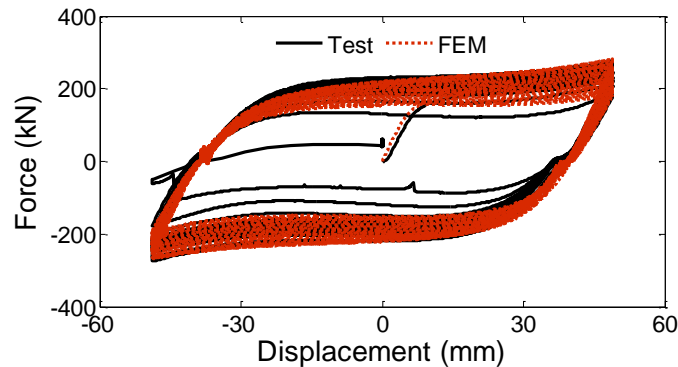


Figure 26: Experimental and numerical hystereses of SSD-WHP1 under CA at $7u_y$

This model will be used to study the fracture behaviour of SSD-WHPs. The parameters that define the fracture criteria (namely ductile damage and damage evolution in Abaqus Explicit) will be validated against the CNS tests and the full component tests. The fracture model will be then used to predict the fracture of SSD-WHPs under any loading protocol.

6 CONCLUSIONS

Duplex stainless steel seismic dampers with an hourglass shape, named SSD-WHPs, were used in a novel CBF-MRF to reduce residual drifts after a strong earthquake, taking advantage of their high post-yield stiffness. The SSD-WHPs were further validated in this study by means of full scale components tests replicating the loading and boundary conditions of a braced frame. The hardening and fracture parameters of duplex stainless steel were identified performing coupon tests on round and circumferentially-notched bars. Based on the results presented herein, the following conclusions are drawn:

- SSD-WHPs possess excellent ductility and fracture capacity under cyclic loading. They pass the standard protocol for braced frames and they are able to sustain much larger cyclic deformations than those expected under the maximum considered earthquake.
- The optimised hourglass shape of the SSD-WHPs results in a widespread distribution of plastic strains over their length and in a significant axial elongation.
- Coffin-Manson relationships are calibrated for the two geometries of SSD-WHPs. The linear damage accumulation model (Miner's rule) gives an acceptable estimation of fracture under random loading protocols.
- SSD-WHPs do not fracture under excessive monotonic loading, indicating that they are able to provide enhanced ductility and robustness to a frame in progressive collapse loading conditions.
- Accurate cyclic hardening parameters of the material were identified using the results from monotonic and cyclic tests on round and circumferentially-notched bars. Complementary finite element analyses provided a good correlation with the experimental tests.
- A finite element model of the SSD-WHPs developed using Abaqus Explicit showed an excellent agreement with the test. By using the results from the coupon tests, the fracture parameters will be identified and used to develop fracture simulations of SSD-WHPs subjected to any cyclic loading. Collapse simulations of the proposed frame with SSD-WHPs will be then carried out.

REFERENCES

- [1] Clifton G.C., Nashid H., Ferguson G., Hodgson M., Seal C., Bruneau M., MacRae G.A. and Gardiner S., “Performance of eccentrically braced framed buildings in the Christchurch earthquake series of 2010/2011”, Proceedings of the 15th World Conference on Earthquake Engineering (15 WCEE), Lisbon, Portugal, Paper 2502, 2012.
- [2] Skinner R.I., Kelly J.M. and Heine A.J., “Hysteretic dampers for earthquake-resistant structures”, *Earthquake Engineering & Structural Dynamics*, 3, 287-296, 1974.
- [3] Whittaker A.S., Bertero V.V., Thompson C.L. and Alonso L.J., “Earthquake simulator testing of steel plate added damping and stiffness elements”, Technical Report, Earthquake Engineering Research Center, University of California, Berkeley, CA, 1989.
- [4] Tsai K.C., Chen H.W., Hong C.P. and Su Y.F., “Design of steel triangular plate energy absorbers for seismic-resistant construction”, *Earthquake Spectra*, 9, 505-528, 1993.
- [5] Kajima, *Honeycomb Damper System*, Japan, Kajima Corporation, 1991.
- [6] Vayas I. and Thanopoulos P., “Innovative dissipative (INERD) pin connections for seismic resistant braced frames”, *International Journal of Steel Structures*, 5, 453-464, 2005.
- [7] Gray M., Christopoulos C. and Packer J., “Cast steel yielding brace system for concentrically braced frames: concept development and experimental validations”, *Journal of Structural Engineering*, 140, 04013095, 2014.
- [8] Iwata M., Kato T. and Wada A., “Buckling-restrained braces as hysteretic dampers”, Proceedings of 3rd International Conference STESSA, Montreal, Canada, 2000.
- [9] McCormick J., Aburano H., Ikenaga M. and Nakashima M., “Permissible residual deformation levels for building structures considering both safety and human elements”, Proceedings of 14th World Conference on Earthquake Engineering, Beijing, China, 2008.
- [10] Watanabe A., Hitomi Y., Saeki E., Wada A. and Fujimoto M., “Properties of brace encased in buckling-restraining concrete and steel tube”, Proceedings of 9th World Conference on Earthquake Engineering, Tokyo-Kyoto, Japan, 1988.
- [11] Bruneau M., Uang C.M. and Sabelli R., *Ductile design of steel structures*, McGraw Hill, Inc, 2011.
- [12] Erochko J., Christopoulos C., Tremblay R. and Choi H., “Residual drift response of SMRFs and BRB frames in steel buildings designed according to ASCE 7-05”, *Journal of Structural Engineering*, 137, 589-599, 2011.
- [13] Pettinga D., Christopoulos C., Pampanin S. and Priestley N., “Effectiveness of simple approaches in mitigating residual deformations in buildings”, *Earthquake Engineering & Structural Dynamics*, 36, 1763-1783, 2008.
- [14] Baiguera M., Vasdravellis G. and Karavasilis T.L., “Dual seismic-resistant steel frame with high post-yield stiffness energy-dissipative braces for residual drift reduction”, *Journal of Constructional Steel Research*, 122, 198-212, 2016.
- [15] Vasdravellis G., Karavasilis T.L. and Uy B., “Large-scale experimental validation of steel posttensioned connections with web hourglass pins”, *Journal of Structural Engineering*, 139, 1033-1042, 2013.
- [16] Vasdravellis G., Karavasilis T.L. and Uy B., “Design rules, experimental evaluation, and fracture models for high-strength and stainless steel hourglass shape energy dissipation devices”, *Journal of Structural Engineering*, 140, 04014087, 2014.
- [17] Shen Y., Christopoulos N., Mansour C. and Tremblay R., “Seismic design and performance of steel moment-resisting frames with nonlinear replaceable links”, *Journal of Structural Engineering*, 137, 1107-1017, 2014.
- [18] *Eurocode 3: Design of Steel Structures - Part 1-1: General Rules and Rules for Building*, CEN, Brussels, European Committee for Standardization, 2004.

- [19] *Eurocode 8: Design Provisions for Earthquake Resistance of Structures - Part 1: General Rules, Seismic Actions and Rules for Building*. CEN, Brussels, European Committee for Standardization, 2004.
- [20] *Metallic Materials. Tensile Testing. Part 1: Tests at ambient temperature*. EN 1002-1, CEN, Brussels, European Committee for Standardization, 2001.
- [21] Smith C.M., Deierlein G.G. and Kanvinde A.M., “A stress-weighted damage model for ductile fracture initiation in structural steel under cyclic loading and generalized stress states”, Technical Report, The John A. Blume Earthquake Engineering Center, Stanford University, 2014.
- [22] *Seismic Provisions for Structural Steel Buildings*. ANSI/AISC 341-10, Chicago, AISC, 2010.
- [23] McKenna F., Fenves G., Scott M., and Jeremic B., *Open System for Earthquake Engineering Simulation (OpenSees)*. Pacific Earthquake Engineering Research Center, University of California, Berkley, CA, 2000.
- [24] Hibbit D., Karlsson B. and Sorensen P., *ABAQUS users’ manual*. 6.14 edition, Providence, RI, 2013
- [25] Kanvinde A.M. and Deierlein G.G., “The void growth model and the stress modified critical strain model to predict ductile fracture in structural steel”, *Journal of Structural Engineering*, 132, 701-712, 2006.